Experimental Investigation and RSM Optimization of Nd:YAG laser Processing Parameters for Sol-Gel Deposited Hydroxyapatite-Titanium dioxide Coated SS 316L stainless steel

Prakash Sekar[1*], *SurendraBabu Kuppuswam*[1], Nallusamy Sellappa[2], *Muruganandham Balakrishnan*[1] and *Manigandan Mahalingam*[1]

[1]Department of Mechanical Engineering, Aarupadai Veedu Institute of Technology, Vinayaka Mission's Research Foundation, Deemed to be University, Tamil Nadu, India.
[2]Department of Adult, Continuing Education and Extension, Jadavpur University, Kolkata, India

Abstract. The research focuses on Response Surface Methodology (RSM) to optimise process parameters for HA-TiO_2 nanocomposite coatings on SS 316L substrates, organised using the sol-gel method and modified with Nd:YAG laser surface treatment. Four process variables (cutting speed, nozzle height, peak power and duty cycle) was carefully adjusted using RSM to determine their impact on surface roughness (Ra), heat impacted zone (HAZ) and kerf deviation. A central composite design with 30 experimental trials was used to create credible predictive models and examine parameter interactions. The results find that higher laser power and duty cycle (%) with lower scan speeds leads to higher Ra and thicker coatings, while moderate laser energy with optimal scan speed generates smoother, more uniform and adherent coatings.The measured Ra levels varied from 18.50 µm to 29.77 µm, with lower roughness at higher scan speeds and reduced power and higher roughness at low scan speeds and increased power. Heat-affected zone (HAZ) ranged from 0.573 mm to 2.204 mm and kerf deviation ranged from 0.355 mm to 0.841 mmwhich increased with larger thermal input. The optimised lasersol-gel parameters improve the useful, structural and tribological properties of HA-TiO_2-coated SS 316L surfaces which show them suitable for biomedical implant applications.

1 Introduction

Among the most commonly used biomaterials is stainless steel 316L because of its high mechanical strength, corrosion resistance as well as biocompatibility [1]. But its bioinert surface does not interact directly with bone tissue and surface modification is needed to

*Correspondingauthor:prakash.mech94@gmail.com

increase bone bonding and durability in physiological conditions [2]. Hydroxyapatite (HA) has been given much attention in the recent years with its lot coating materials as the similarity between its chemical properties and real bone mineral is given a lot of attention because of its great bioactivity. Introduction of titanium dioxide (TiO2) into HA coatings enhances mechanical strength, corrosion resistance as well as biological responsiveness [3]. The sol-gel method has been found to be an expedient way to prepare such coatings which can be controlled well at a low cost of processing, with a fine control of stoichiometry and microstructure and can produce uniform and adherent layers at relatively low processing temperatures [4] sol-gel references. Sol-gel coatings are typically typified by low crystallinity and inadequate substrate adhesion in their deposited form, and this may adversely affect the performance of the coating [5-7]. Improvements in coating density and adhesive strength are normally accomplished with post-deposition treatments in an attempt to overcome these challenges [8-9]. A post-processing technique that has proven to be effective is the Nd:YAG laser surface treatment that can provide targeted heating in a relatively short time. It is a method that enhances crystallinity and decreases porosity and coating-substrate adhesion without creating large amounts of thermal damage [11] works of paramount importance in laser surface treatment. The performance of HA-TiO2 coatings is not yet well comprehended in terms of the effect of laser processing parameters such as power, scanning speed and pulse frequency on the performance of the laser processing [12-13].

Earlier studies have mainly concentrated on individual parameters with limited research being conducted on interaction between multiple parameters which refer to studies with limited parameter analysis [14-18]. The research uses Response Surface Methodology (RSM) in the analysis and optimization of laser treatment parameters in order to make HA-TiO2 coating on SS 316L substrates. Laser power, scanning speed and duty cycle (%) are investigated to determine their effect on significant responses like surface roughness, hardness and corrosion resistance to come up with a prediction model. The findings help determine the right processing conditions in order to produce superior implant coating.

2 Materials and Methodology

The substrate that was chosen and was SS 316L stainless steel because it has excellent resistance to corrosion and confirmed biocompatibility [19]. Mechanical polishing was applied to the samples to get a smooth surface and acetone and ethanol ultrasonic cleaning were applied in the samples to eliminate contaminants.

The nanocomposite of HA-TiO2 coating was prepared using sol-gel technique. The TiO2 precursor was titanium iso prop oxide and the calcium and phosphorus to produce hydroxyapatite were supplied by calcium nitrate tetrahydrate and ammonium dihydrogen phosphate. Careful pH and molar ratios were used to synthesise the sol and then another step taken to stabilise the solutions.

The sol was applied to the cleaned SS 316L substrates by dip coating, with coating cycles and removal speed regulated to ensure a uniform coating thickness. To increase coating quality and promote crystallisation, the coated samples were heated and cooled. The surface was treated with a Nd:YAG laser (λ = 1064 nm) to improve coating-substrate bonding and microstructure. To examine their effect on coating properties, RSM design was used to change laser power, scanning speed and duty cycle (%) [20].

This study evaluates laser processing reactions of HA-TiO_2 coated SS 316L specimens by measuring surface roughness (Ra), heat affected zone (HAZ) and kerf deviation using RSM-designed experiments [21]. Vickers testing was utilised to determine hardness, while a Coordinate Measuring Machine (CMM) was employed to determine surface roughness. Electrochemical impedance spectroscopy (EIS) and potential dynamic polarisation have

been used to assess corrosion performance. RSM optimisation of the laser parameters was carried out utilising the results of these tests [22].

3 Experimental Design

Response Surface Methodology (RSM) is used in this study experimental design to optimise the HA-TiO_2 nanocomposite coating process on SS 316L surfaces [23]. The study was conducted in two phases, initial, the coating was applied using the sol-gel technique and then a Nd:YAG laser was used for post-processing. Laser power, scanning speed and duty cycle (%) are the three laser treatment parameters that are optimised at three different levels. This method makes it possible to create a quadratic model that describes why laser settings related to performance metrics like corrosion resistance and surface roughness. This technique can be used to identify the best processing parameters for producing a consistent coating with enhanced qualities [24]. Table 1 and table 2 shows the input and ouput parameters.

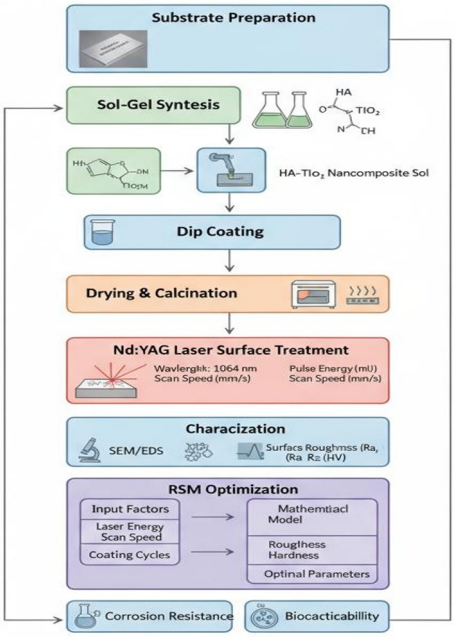

Fig. 1. Experimental factor-levels for HA-TiO2 Nanocomposite coting RSM optimisation.

Table 1. Input Parameters

Factor	Low	Center	High	Units
Cut speed	1.0	2.5	5.0	m/min
Nozzle height	0.2	0.8	1.5	mm
Peak power	20	45	100	% (or W)
Duty cycle	20	50	100	%

Fig. 2. Metrological Setup for Geometrical and Surface Analysis of Coated Samples.

3.1 Surface Roughness (Ra)

In analysing components made by additive manufacturing, surface roughness is a crucial factor. The manufactured samples macro- and micro-geometrical properties were measured using a Coordinate Measuring Machine (CMM), such as the ZEISS CONTURA, fitted with the proper probing mechanism. surface roughness (Ra) and maximum profile height (Rz), two important surface metrics, are outlined in Figure 3 (a), coupled with the CMM setup utilised for measurement. These characteristics, which affect tribological behaviour, fatigue strength and visual quality, are frequently employed to characterise surface condition. In addition, as shown in Figures 3 (b) and 3(c), the same CMM was used to confirm additional geometric properties, such as roundness and flatness.This detailed dimensional assessmentprovides a basis for relating process conditions with the resulting surface finish and dimensional precisionof the manufactured parts.

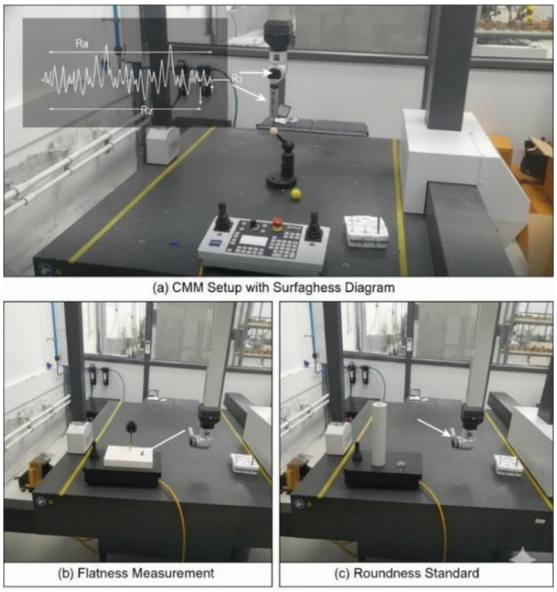

Fig. 3. Surface Roughness.

3.2 Heat Affected Zone (HAZ)

The heat-affected zone characterises the region adjacent to the laser-cut surface which undergoes microstructural changes due to the thermal energy reported during cutting. The extent of this zone is influenced by the amount of heat conducted into the material relative to the rate of material removal. The HAZ is generally proportional to the ratio of laser power to the product of cutting speed and focal distance

$$HAZ \propto \frac{p}{v.f} \quad (1)$$

where
P= Laser power
v= Cutting speed
t= Material thickness

3.3 Kerf Deviation

Kerf deviation difference in the width of the cut, is chieflyruled by the energy density delivered to the material and the precision of beam focusing. The similar proportional relationship to the heat input parameters

$$Kerf \propto \frac{p}{v.f} \quad (2)$$

where
P= Laser power
v= Cutting speed
f= Focal distance or nozzle gap

Table 2. Output Parameters

Run	A: Cut speed (m/min)	B: Nozzle height (mm)	C: Peak power %	D: Duty cycle %	Ra (µm)	HAZ (mm)	Kerf deviation (mm)
1	3	0.6	20	100	21.27	1.215	0.394
2	3	0.6	60	60	22.98	1.337	0.542
3	3	0.6	40	40	21.09	0.92	0.418
4	3	1	20	60	21.24	0.871	0.355
5	5	0.6	60	20	19.11	0.965	0.467
6	1	0.2	60	60	25.58	1.36	0.586
7	5	0.2	60	60	19.69	1.323	0.526
8	3	0.6	100	20	25.24	1.474	0.712
9	5	0.6	100	60	23.55	1.816	0.74
10	3	0.2	60	100	24.22	1.711	0.627
11	1	0.6	100	60	29.77	1.862	0.812
12	3	0.6	100	100	28.08	2.204	0.841
13	3	0.6	60	80	24.79	1.547	0.617

14	5	0.6	20	60	18.5	0.87	0.361
15	1	0.6	60	20	26.21	1.032	0.574
16	5	0.6	40	100	21.32	1.475	0.526
17	5	1	60	60	22.47	1.366	0.579
18	3	1	100	60	28.38	1.869	0.815
19	3	0.2	60	20	22.81	1.015	0.554
20	3	0.6	80	40	25.76	1.446	0.691
21	1	1	60	60	28.91	1.417	0.66
22	1	0.6	20	60	25.38	0.931	0.46
23	3	0.2	100	60	27.25	1.866	0.827
24	3	1	60	100	27.44	1.765	0.697
25	1	0.6	60	100	29.71	1.78	0.729
26	3	0.2	20	60	21.98	0.914	0.44
27	3	0.6	80	100	28.33	2.005	0.805
28	3	0.6	80	80	27.84	1.828	0.782
29	3	1	60	20	25.59	1.058	0.607
30	3	0.6	20	20	22.06	0.573	0.406

4 Results and Discussion

4.1 Response of Surface Roughness (Ra)

Surface roughness (Ra) was experimentally acquired with numerous parameters of the process, such as cut speed, nozzle height, maximum power and duty cycle. The findings evidently demonstrated an overall impact on the quality of surfaces. Figure 4 (a) shows the correlation between cut speed and nozzle height, whereby cut speeds of higher magnitude (5 m/min) tend to give smoother surfaces, whereas, lower cut speeds (1-3 m/min), coupled with a middle range nozzle height (0.6-1 mm) will give a higher Ra value. Figure 4 (b) is a combination of cut speed and peak power and indicates that the enhancement of Ra, especially at low cut speeds, correlates with an increase in peak power past 60% and that at that point the thermal effects become predominant. Figure 4 (c) demonstrates the effect of the duty cycle on Ra and higher duty cycle (80-100% when used with larger cut speeds which increases the surface roughness) leads to higher values of the Ra whereas smaller cut cycle (20-40% cut cycle) leads to lower values of the Ra. The integrated effects of nozzle height on maximum power and duty cycle are presented in figs. 4(d) and (e) respectively. The rise in ra is proportional to the rise in power level and the best combinations of reduced nozzle height and moderate nozzle duty curves reduce the uneven surfaces. Figure 4 (f) represents the interaction between peak power and duty cycle and this illustrates the importance of having a balance between peak power and high duty cycles as more peak power and high duty cycles would produce the roughest surfaces. It is found that cut speed, nozzle height, peak power and duty adjustments are needed to achieve low surface

roughness and this presents useful information on how the process can be optimised in laser cutting operations.

$$Ra = 24.0422 + -3.25545 * A + 1.04167 * B + 2.81376 * C + 1.20916 * D + -0.1375 * AB + 0.088004 * AC + 0.141158 * AD + 0.4675 * BC + 0.11 * BD + 0.870171 * CD + -0.0326886 * A\hat{}2 + 0.405483 * B\hat{}2 + 0.125353 * C\hat{}2 + 0.45427 * D\hat{} \quad (3)$$

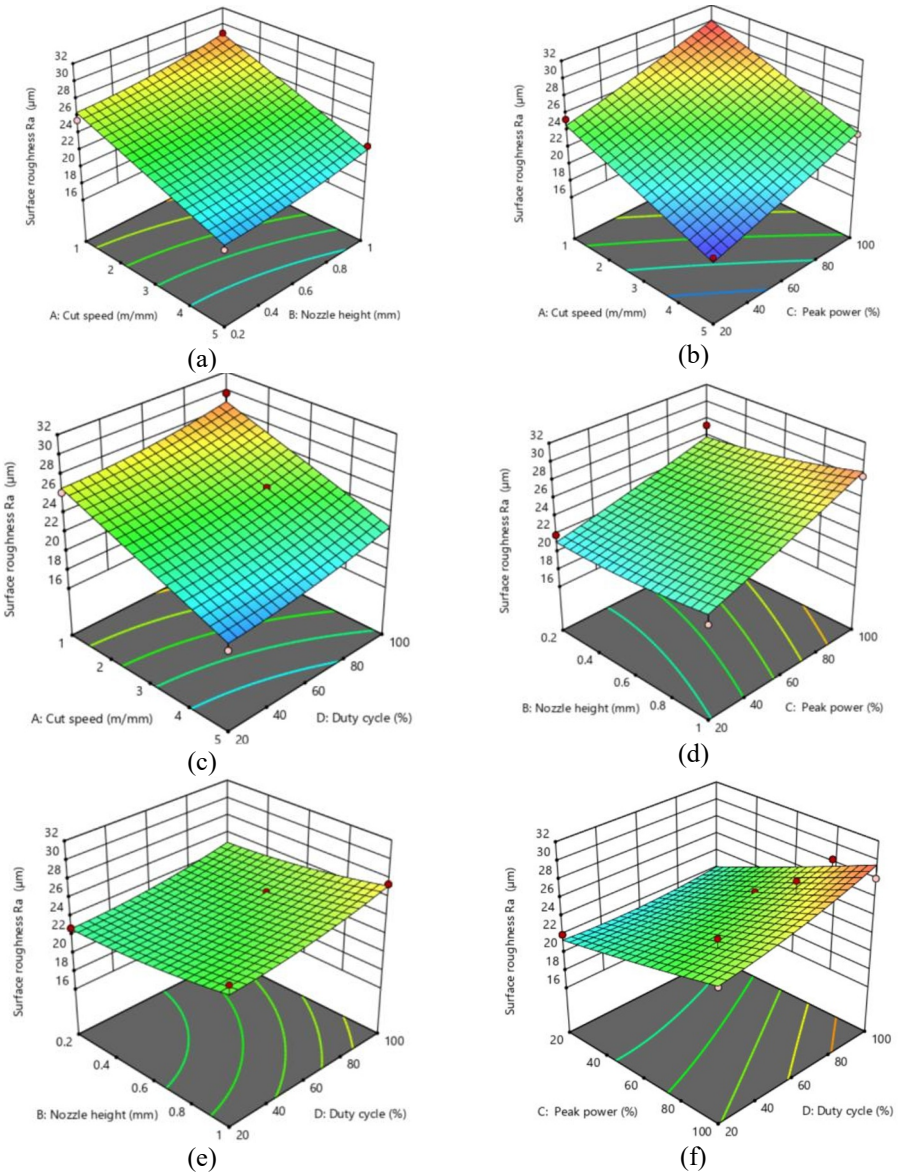

Fig. 4. (a) Surface Roughness (Ra) - Cut Speed vs Nozzle Height (b) Ra - Cut Speed vs Peak Power, (c) Ra - Cut Speed vs Duty Cycle, (d) Ra -Nozzle Height vs Peak Power, (e) Ra -Nozzle Height vs Duty Cycle, (f) Ra - Peak Power vs Duty Cycle

4.2 Response of Heat Affected Zone

Investigation on the heat-affected zone (HAZ) under multiple process parameters, including duty cycle, peak power, nozzle height and cut speed, shows clear patterns that are helpful for selecting appropriate laser cutting conditions. Figure 5 (a) illustrates the combined effect of cut speed and nozzle height. It shows that lower cut speeds (1-3 m/min) with smaller nozzle heights (0.2-0.6 mm) generally result in lower HAZ values, while larger nozzle heights (1 mm) slightly improve heat penetration. HAZ significantly rises at higher peak powers (80-100%), especially at moderate cut speeds, indicating higher power levels and increased heat input, as seen in Figure 5 (b), which shows the relationship between peak power and cut speed. Figure 5 (c) shows the relationship between duty cycle and cut speed. At intermediate cut speeds, larger duty cycles (80-100%) increase HAZ production, while lower duty cycles (20-40%) minimise thermal spread. Figures 5 (d) and (e) show the combined impact of nozzle height on peak power and duty cycle, correspondingly. High nozzle height and peak power or high duty cycle seem to produce the most HAZ, while lower nozzle heights combined with moderate power or duty cycle appear to generate the lowest HAZ. The relationship between duty cycle and peak power is finally shown in Figure 5 (f), which shows that concurrent increases in both parameters lead to the largest HAZ due to increased heat input and prolonged energy exposure. The results show that controlling cut speed, nozzle height, peak power and duty cycle in a balanced manner is important to minimize HAZ, leading to improved cutting accuracy and better thermal controlduring laser processing operations.

$$HAZ = 1.36342 + -0.0263416 * A + 0.0130833 * B + 0.480379 * C + 0.360356 * D + -0.0035 * AB + 0.00187359 * AC + 0.00322522 * AD + 0.0115 * BC + 0.00275 * BD + 0.0211424 * CD + -0.000865979 * A\text{^}2 + 0.0100214 * B\text{^}2 + 0.00318711 * C\text{^}2 + 0.0110911 * D\text{^}2 \quad (4)$$

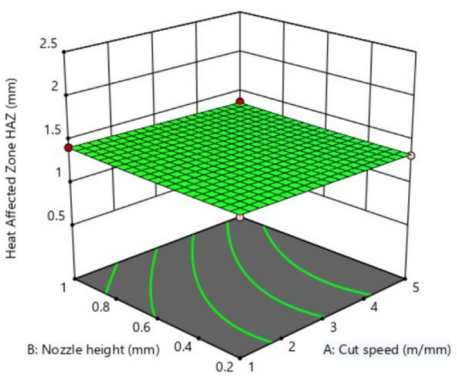

(a)

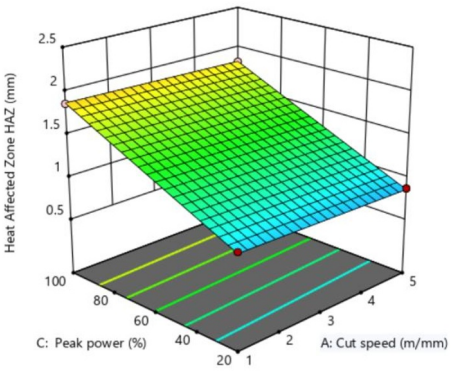

(b)

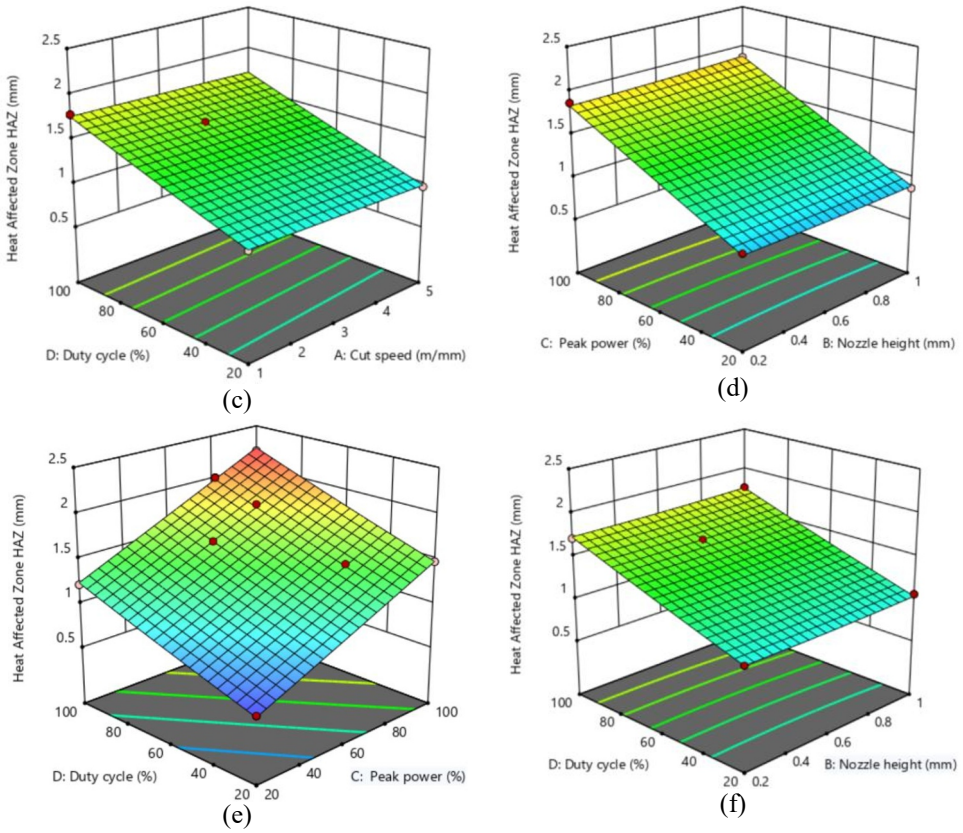

Fig. 5. (a) Heat-affected zone- Cut Speed vs Nozzle Height (b) HAZ- Cut Speed vs Peak Power, (c) HAZ- Cut Speed vs Duty Cycle, (d) HAZ-Nozzle Height vs Peak Power, (e) HAZ-Nozzle Height vs Duty Cycle, (f) HAZ- Peak Power vs Duty Cycle

4.3 Response of kerf deviation

During laser cutting operations, dimensional accuracy and process stability are evaluated by evaluating kerf deviation under various process parameters, including cut speed, nozzle height, peak power and duty cycle. The effect of cut speed and nozzle height is shown in Figure 6 (a), where kerf deviation is minimised at low cut speeds (3 m/min) with smaller nozzle heights (0.2-0.6 mm) and higher nozzle heights (1 mm) slightly increase deviation, suggesting lower precision at higher standoff distances. The combined effect of cut speed and peak power can be seen in Figure 6 (b), where kerf deviation rises with larger peak powers (80-100%), especially at medium cut speeds. This indicates that too much heat input causes kerf widths to become broader and more irregular. The effect of duty cycle can be seen in Figure 6 (c), as smaller duty cycles (20-40%) preserve kerf consistency while higher duty cycles (80-100%) at moderate cut speeds generate greater variances. Maximum kerf deviation is seen at high nozzle heights combined with elevated power or duty cycle, while appropriate combinations of lower nozzle heights with moderate power or duty cycle minimise variations. Figures 6 (d) and (e) show the combined effect of nozzle height with peak power and duty cycle, accordingly. The impact of peak power and duty cycle is shown in Figure 6 (f), as shows that concurrent increases in both parameters result in the biggest kerf deviations because of increased material melting and unstable cutting. The results

shows that proper control ofcut speed, nozzle height, peak power and duty cycle is crucial for achieving minimal kerf deviation, leading to improved dimensional accuracy and cutting quality in laser cutting processes. Table 3 shows the anova results.

$$Kerf = 0.583318 + -0.0420159 * A + 0.01275 * B + 0.200518 * C + 0.0563153 * D + -0.00525 * AB + 0.00373963 * AC + 0.00545233 * AD + 0.01825 * BC + 0.00425 * BD + 0.0337901 * CD + -0.00130546 * A^2 + 0.0155934 * B^2 + 0.00485898 * C^2 + 0.0179619 * D^2 \quad (5)$$

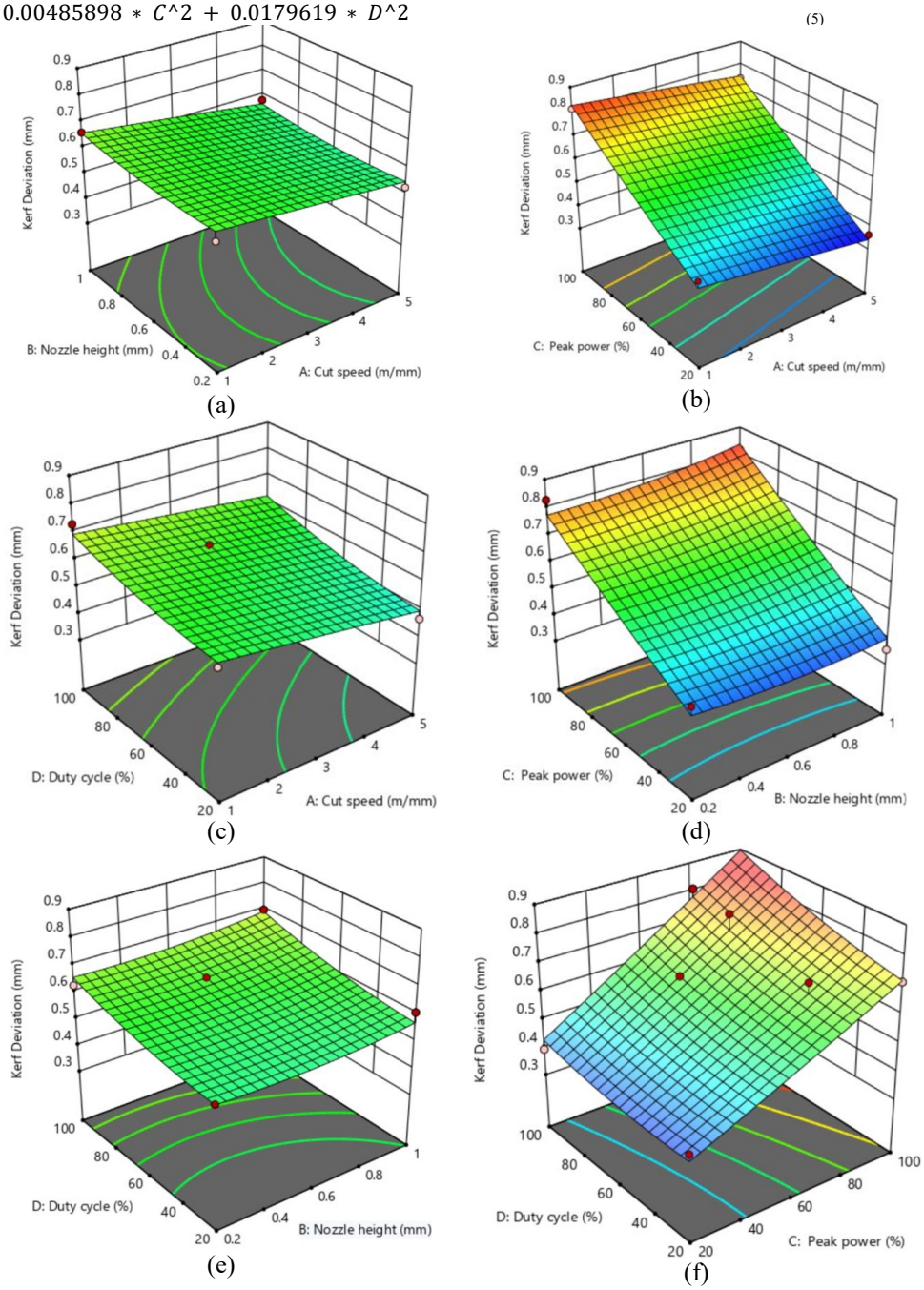

Fig. 6. (a) Kerf- Cut Speed vs Nozzle Height (b) Kerf- Cut Speed vs Peak Power, (c) Kerf- Cut Speed vs Duty Cycle, (d) Kerf-Nozzle Height vs Peak Power, (e) Kerf-Nozzle Height vs Duty Cycle, (f) Kerf- Peak Power vs Duty Cycle

Table 3. Anova - RA, HAZ and Kerf

Source	**Surface Roughness (Ra) µm**			**HAZ (mm)**			**Kerf Deviation (mm)**		
	Sum of Squares	F-value	p-value	Sum of Squares	F-value	p-value	Sum of Squares	F-value	p-value
Model	286.68	15.88	<0.0001	4.98	455.64	<0.0001	0.6277	22.76	<0.0001
A - Cut speed	125.73	97.53	<0.0001	0.0082	10.54	0.0054	0.0209	10.63	0.0053
B - Nozzle height	13.02	10.10	0.0062	0.0021	2.63	0.1257	0.0020	0.99	0.3355
C - Peak power	103.12	79.99	<0.0001	3.01	3846.96	<0.0001	0.5237	265.83	<0.0001
D - Duty cycle	20.23	15.69	0.0013	1.80	2299.79	<0.0001	0.0439	22.28	0.0003
AB	0.0756	0.0587	0.8119	0.0000	0.0627	0.8056	0.0001	0.0560	0.8162
AC	0.0318	0.0247	0.8773	0.0000	0.0184	0.8938	0.0001	0.0291	0.8667
AD	0.0771	0.0598	0.8102	0.0000	0.0515	0.8236	0.0001	0.0584	0.8124
BC	0.8742	0.6781	0.4231	0.0005	0.6771	0.4235	0.0013	0.6763	0.4238
BD	0.0484	0.0375	0.8490	0.0000	0.0387	0.8466	0.0001	0.0367	0.8507
CD	3.42	2.66	0.1239	0.0020	2.59	0.1285	0.0052	2.62	0.1263
A^2	0.0064	0.0049	0.9449	4.463E-06	0.0057	0.9408	0.0000	0.0051	0.9437

B^2	0.9794	0.7597	0.3972	0.0006	0.7657	0.3953	0.0014	0.7352	0.4047
C^2	0.0825	0.0640	0.8037	0.0001	0.0683	0.7974	0.0001	0.0630	0.8053
D^2	1.06	0.8240	0.3784	0.0006	0.8106	0.3822	0.0017	0.8431	0.3730
Residual	19.34	-	-	0.0117	-	-	0.0295	-	-
Cor Total	306.02	-	-	5.00	-	-	0.6573	-	-
R^2	0.9368	-	-	0.9976	-	-	0.9549	-	-

5 Conclusion

The study identified the optimum laser processing for Hydroxyapatite - Titanium dioxide coated SS 316L stainless steel using RSM, with importance on minimizing surface roughness, kerf deviation and thermal influence during post-coating machining:

- Surface Roughness (Ra): Lowest Ra of 18.50 µm was observed at Run 14 (Cut speed: 5 m/min, Nozzle height: 0.6 mm, Peak power: 20%, Duty cycle: 60%), while the highest Ra of 29.77 µm occurred at Run 11 (Cut speed: 1 m/min, Nozzle height: 0.6 mm, Peak power: 100%, Duty cycle: 60%).
- Heat-Affected Zone (HAZ): Minimum HAZ of 0.573 mm was recorded at Run 30 and maximum HAZ of 2.204 mm occurred at Run 12, showing that higher thermal input increases HAZ (high power and duty cycle) increases HAZ.
- Kerf Deviation: The lowest kerf deviation of 0.355 mm was experiential at Run 4, the maximum deviation of 0.841 mm occurred at Run 12, shows that extreme laser settings reduce dimensional accuracy.
- The higher cut speeds with moderate power and duty cycle produced smoother surfaces, lower HAZ and improved kerf accuracy, the low speeds with high power and duty cycle led to rougher surfaces, larger thermal effects and higher kerf deviation

References

1. M.T. Mohammed, A.H. Lafta, F.Q. Mohammed. Surface characterization of pure and composite sol-gel nano-coatings deposited on 316L stainless steel for hard tissue replacements. Mater. Res. 26 (2023) e20220479.
2. T.H. Qaid. Properties of Eggshell-Derived Hydroxyapatite Coatings on Titanium Produced by Micro-Arc Oxidation Method. Master's Thesis, University of Malaya, Malaysia (2019).
3. R. Ahmadi, A. Afshar. In vitro study: Bond strength, electrochemical and biocompatibility evaluations of TiO_2/Al_2O_3 reinforced hydroxyapatite sol-gel coatings on 316L SS. Surf. Coat. Technol. 405 (2021) 126594.
4. E.H. Purwanto, R. Lukiawan, B.B. Louhenapessy, B. Basuki, P. Anggraeni, N.T.E. Darmayanti. Corrosion Resistant Support Materials (CRSM) as potential development

of technical parameters for biocompatibility testing of bone implant products: A review. J. Sains Mater. Indones. 26 (2024) 11-23.

5. Tayyeh, A. K., & Hasan, A. F. (2026, February). Enhancing 316L stainless steel for biomedical applications: Advances in surface coatings. In AIP Conference Proceedings (Vol. 3379, No. 1, p. 060027). AIP Publishing LLC.
6. N.S. Radhi, A.J. Salman, Z. Al-Khafaji. Investigation of in vitro behavior of composite coating hydroxyapatite-nano silver on 316L stainless steel substrate by electrophoretic technique for biomedical tools. Open Eng. 14 (2024) 20240017.
7. A.E. Tudose. NiCrAlY layers performance assessment developed onto 310H alloy by EB-PVD method after oxidation in aggressive conditions. NanoBioMat 2024 - Summer Ed. 5 (2024) 45.
8. Mohammadsadegh, A., Allahkaram, S. R., & Gharagozlou, M. (2025). Electrophoretic deposition of chitosan/gelatin/hydroxyapatite nanocomposite coatings on 316 L stainless steel for biomedical applications. Biomedical Materials, 20(1), 015020.
9. M.R. Shirdar, et.al. Hydroxyapatite-titania nanotube composite as a coating layer on Co-Cr-based implants: Mechanical and electrochemical optimization. Ceram. Int. 42 (2016) 6942-6954.
10. Pauline, S. A., Karuppusamy, I., Gopalsamy, K., &Nallaiyan, R. (2025). Template assisted fabrication of nanoporous titanium dioxide coating on 316 L stainless steel for orthopaedic applications. Journal of the Taiwan Institute of Chemical Engineers, 166, 105576.
11. Ö. Canpolat, A. Çanakçı, G.G. Gültekin. Effect of HA ratio on the morphology and characteristics of Ti-HA composite coatings on Ti6Al4V-ELI synthesized via mechanical milling. Tribol.-Mater. Surf. Interfaces 18 (2024) 245-255.
12. M. Al-Amin, A.M.A. Rani, A.A.A. Aliyu, M.G. Bryant, M. Danish, A. Ahmad. Bio-ceramic coatings adhesion and roughness of biomaterials through PM-EDM: A comprehensive review. Mater. Manuf. Process. 35 (2020).
13. A.R. Rafieerad, A.R. Bushroa, B. Nasiri-Tabrizi, S. Baradaran, S. Shahtalebi, S. Khanahmadi, W.J. Basirun. In-vitro bioassay of electrophoretically deposited hydroxyapatite-zirconia nanocomposite coating on Ti-6Al-7Nb implant. Adv. Appl. Ceram. 116 (2017) 293-306.
14. B. Singh, G. Singh, B.S. Sidhu. Investigation of the in vitro corrosion behavior and biocompatibility of niobium (Nb)-reinforced hydroxyapatite (HA) coating on CoCr alloy for medical implants. J. Mater. Res. 34 (2019) 1678-1691.
15. A.S. Hammood. Biomineralization of 2304 duplex stainless steel with surface modification by electrophoretic deposition. J. Appl. Biomater. Funct. Mater. 18 (2020) 2280800019896215.
16. M. Krishani, H. Suhaimi, N.S. Sambudi. A review of hydroxyapatite: Sustainable product development in terms of waste valorization. In: What to Know About Hydroxyapatite. Nova Science Publishers (2023) 219-243.
17. M. Furko, K. Balázsi, C. Balázsi. Calcium phosphate loaded biopolymer composites—A comprehensive review on the most recent progress and promising trends. Coatings 13 (2023) 360.
18. E. Matei, A.A. Ștăulean, M. Petriceanu, M. Râpă, R.R. Piticescu, R. Ștefănoiu, C. Predescu. Environmental sustainability based on zirconium dioxide utilization in non-conventional energy applications. Environments 11 (2024) 265.

19. A. Afzal. Implantable zirconia bioceramics for bone repair and replacement: A chronological review. Mater. Express 4 (2014) 1-12.
20. A.O. Oluwatosin. Surface Morphology Characterisation: Magnetron Sputtering of Nanostructured Titanium Carbide Thin Films on Titanium and its Alloys. Doctoral Dissertation, University of Johannesburg, South Africa (2020).
21. R. Ikram, B.M. Mohamed Jan, M.A. Abdul Qadir, A. Sidek, M.M. Stylianakis, G. Kenanakis. Recent advances in chitin and chitosan/graphene-based bio-nanocomposites for energetic applications. Polymers 13 (2021) 3266.
22. G. Basmacı. Optimization of machining Nilo 36 superalloy parameters in turning operation. Open Chem. 21 (2023) 20220276.
23. G. ALMisned, E. Rabaa, D. Sen Baykal, E. Ilik, G. Kilic, H.M. Zakaly, H.O. Tekin. The impact of chemical modifications on gamma-ray attenuation properties of some WO_3-reinforced tellurite glasses. Open Chem. 21 (2023) 20220297.
24. G. ALMisned, E. Rabaa, D. Sen Baykal, E. Ilik, G. Kilic, H.M. Zakaly, H.O. Tekin. Translocation of tungsten (VI) oxide/gadolinium (III) fluoride in tellurite glasses towards improvement of gamma-ray attenuation features in high-density glass shields. Open Chem. 21 (2023) 20220289